Published in final edited form as:
J Control Release. 2006 March 10; 111(1-2): 128–134.

Ultrasound Radiation Force Enables Targeted Deposition of Model Drug Carriers loaded on Microbubbles

Aaron F H Lum, **Mark A Borden**, **Paul A Dayton**, **Dustin E Kruse**, **Scott I Simon**, and **Katherine W Ferrara***
University of California: Davis, Department of Biomedical Engineering, 451 East Health Sciences Drive, Davis CA 95616

Abstract

A novel drug delivery vehicle is presented that specifically targets using ultrasound radiation force (USRF) and biotin-avidin interactions. Model vehicles consist of avidinated fluorescent nanobeads bound directly to the biotinylated lipid shells of preformed microbubbles. USRF was used to deflect the vehicle from the center of flow to a tube surface in order to facilitate receptor-ligand mediated adhesion. At wall shear stress levels commensurate with venous and arterial flow, USRF was used to direct the vehicles to a biotinylated tube surface. Subsequent high pressure pulses fragmented the carrier, and molecular interactions induced deposition of nanobeads on the wall. Targeting of nanobeads to the tube was molecularly-specific and dependent on, in order of importance, vehicle concentration, wall shear stress, nanobead size, and insonation time. The observation that portions of the microbubble lipid monolayer shell remain attached to adherent nanobeads is important for future consideration of drug transport mechanisms. This versatile method of delivery is shown to enable targeted deposition of nanoparticles in shear flow and could be modified to carry therapeutic agents for controlled release in targeted delivery applications.

Keywords

Microbubble; Ultrasound Radiation Force; Targeted; Drug Delivery; Delivery Vehicle; Nanoparticle

1. Introduction

Success in local delivery of drugs, particularly to tumors, has been limited due to the challenge of targeting diseased tissue in the vasculature while limiting deposition elsewhere. In this study, a new drug delivery vehicle is evaluated which deposits targeted nanoparticles on a surface by adding ultrasound energy. Targeted drug delivery involves the local deposition of therapeutic agents based on active or passive mechanisms. Active targeting requires molecular interactions with disease-specific markers, while passive targeting takes advantage of structural alterations within the particular diseased vasculature [1]. Targeting is advantageous because it increases the local drug concentration in the diseased region while minimizing the deleterious effects of the drug on healthy tissues. Tumors are of particular interest not only because of their clinical significance but also because their angiogenic vasculature exhibits larger junctions between endothelial cells [2], with fenestrations as large as 200 nm observed in many tumors. This "leaky" vasculature, combined with slow lymphatic clearance, enables the accumulation of macromolecules or nanoparticles at the tumor site at a higher concentration than in the plasma [3,4]. Additionally, many angiogenic vessels over-express integrins including $a_v ß_3$ and $a_4 ß_1$ [5,6].

*Corresponding author. Tel.: (530) 754-9436; Fax: (530) 754-5739. *E-mail address*: kwferrara@ucdavis.edu..

Previous studies have explored the use of targeted microbubbles for ultrasound imaging [7–11]. However, the monolayer shell of a lipid-coated microbubble is not an ideal drug reservoir, because it is restricted to specific drug types (i.e., amphiphilic or charged molecules) and in loading capacity by the molecular thickness and surface area [12,13]. Additionally, the circulation time and stability of microbubbles in the bloodstream is short (on the order of ten minutes) [14,15]. Lipids grafted to polyethylene glycol (PEG) or other hydrophilic polymers have been shown to create so-called "stealth" particles that are shielded from the immune system, and hence, increase circulation time [16–19]. However, these particles experience an "accelerated blood clearance" following prior doses that is postulated to be due to increased immune recognition [20–25]. Using microbubbles as a carrier particle and attaching nanoparticles containing a higher payload of drug allows biodistribution of such a carrier particle to be controlled by insonation, using ultrasound pulse schemes which are designed to deflect the vehicle to a target vessel wall and then to rupture the larger lipid carrier. When a traveling ultrasonic wave is absorbed by a particle, the momentum associated with the wave produces a net "primary ultrasound radiation force (USRF)," whereby the radiating sound wave is transferred to the particle. While incompressible objects do experience USRF, compressible objects such as gas bubbles experience far larger forces and are displaced by low-amplitude ultrasound waves [26]. Only recently, however, have researchers examined USRF produced on contrast agent microbubbles with MHz-frequency ultrasound, noting that the resonance frequency of contrast microbubbles is in the frequency range of clinical ultrasound systems, 1–10 MHz [27,28]. A microbubble driven near its resonance frequency experiences a large net USRF in the direction of ultrasound wave propagation. Consequently, pulses of many cycles can deflect resonant microbubbles over distances on the order of millimeters. Thus, it is possible to push contrast agents circulating in the blood pool into contact with targeting sites on a blood vessel wall. When agents are concentrated in the boundary layer near a vessel wall, they travel at a reduced velocity compared to those in the center of the flow stream; this was demonstrated using intra-vital microscopy [29]. In addition to primary USRF, which acts in the direction of acoustic wave propagation, a "secondary USRF" also acts between individual bubbles [28]. For the parameters studied, the net effect of secondary USRF is to cause individual bubbles to attract each other, resulting in a much larger concentration of microbubbles along a vessel wall than might occur otherwise [28]. By localizing microbubbles along a vessel wall with USRF, adhesion efficiency can be improved over 20-fold [10,11].

As a proof of concept, neutravidin-coated fluorescent nanobeads were used to model a nanoparticle drug carrier. Use of these fluorescent beads serves the dual purposes of enabling detection of nanobeads through fluorescence microscopy while also acting as a uniform particle with defined surface chemistry. The carrier particle employed was a biotinylated lipid-shelled microbubble which was then coated with the nanobeads in order to create the delivery vehicle. Cellulose tubes were employed as the vascular model for their transparency to both light and ultrasound, their ability to chemically functionalize their surface, and their predictable flow rate and wall shear stress levels. The experiments described here demonstrate that USRF, at a clinical frequency, and molecular targeting can be used to target these nanoparticles to specific sites at magnitudes of wall shear stress equivalent to those found in the vasculature.

2. Materials and methods

2.1 The model delivery vehicle

The model delivery vehicle was constructed as follows (Fig. 1). 40- or 200-nm diameter yellow-green fluorescent neutravidin-coated latex beads (Fluospheres, Molecular Probes; Eugene, OR) were used as the model drug carrier. Biotinylated, lipid-coated microbubbles were formed using the shaking method as described previously [30]. The lipid shell composition of the microbubbles was 90 mol% 1,2-Distearoyl-*sn*-Glycero-3-Phosphocholine (DSPC), 5 mol%

1,2-Distearoyl-*sn*-Glycero-3-Phosphoethanolamine (DSPE)-Polyethylene Glycol (PEG)2000, and 5 mol% DSPE-PEG2000-Biotin (Avanti Polar Lipids, Inc.; Alabaster, AL). The lipids were mixed in chloroform and dried for ~20 minutes under flowing nitrogen gas. To further dry the lipids, they were heated under vacuum for 45 minutes at 60° C. 0.1 M Tris buffer (Sigma-Aldrich Corp.; St. Louis, MO) was added to the lipids. The solution was placed into a sonic bath for 45 minutes and then aliquoted into gas tight vials to which decafluorobutane gas was added (SynQuest Labs; Alachua, FL). To create fluorescent microbubbles from the lipid solution, the fluorescent lipophilic tracer, DiI (Molecular Probes; Eugene, OR), was added at <1 mol%. Microbubbles were formed by the shaking method using a CAPMIX mixing machine (ESPE; Seefeld, Germany) for 60 seconds. Following formation, microbubble suspensions were washed 3 times and re-suspended in phosphate-buffered saline (PBS; Sigma-Aldrich Corp.; St. Louis, MO) using the flotation method previously described [11,31]. In order to disperse any aggregates, nanobeads were sonicated in a sonic bath (Aquasonic Model 75D; VWR Scientific, West Chester, PA) at power level 9 for 10 minutes prior to incubation with the microbubbles as instructed by the manufacturer (this process did not result in microbubble formation). 40 μL of stock nanobead solution was added to 1 mL of the washed microbubble suspension. The microbubble-nanobead solution was incubated for 10 minutes at room temperature on a mixing apparatus (Orbitron; Boekel Scientific; Feasterville, PA) and then washed three more times. Vehicle concentration was determined by the use of an Accusizer (Particle Sizing Systems Inc.; Santa Barbara, CA). The relative level of nanobead adherence to the microbubbles was determined by flow cytometry using a FACScan (Becton Dickinson; San Jose, CA). Fluorescence microscopy was used to directly visualize the conjugation of the nanobeads to the microbubble shell. Images of the vehicles were obtained using an inverted microscope (Olympus IX71, Melville, NY) interfaced with a video camera (Dage-MTI CCD-300; Michigan City, IN) with a 100X water immersion objective (Carl Zeiss Achroplan 100X, NA 1.0; Thornwood, NY).

2.2 Targeting assay and related ultrasound radiation force parameters

The experimental system consisted of an optically and acoustically transparent 200- micron inner diameter cellulose tube (Spectrum; Los Angeles, CA) submersed in a water bath (Fig. 2). The temperature of the water bath was at ~25° C for all experiments. In order to conduct specific adhesion assays on the cellulose tube, tubes were incubated with cellulose binding domain (CBD)-biotin (~1 mg/ml) overnight (~12 hours) using a standard biotinylation kit following manufacturer's protocols for binding (Sigma-Aldrich Corp.; St. Louis, MO). Tubes were then incubated with 2.5% human serum albumin in order to reduce non-specific adhesion. For the blocking study, vehicles or avidin-coated microbubbles were incubated for >10 minutes at room temperature in 20 μg/mL of biotinylated mouse IgG antibody (Caltag; Burlingame, CA). The concentrations used for nanobead alone studies were determined by measuring the fluorescence of the infranatant of the first vehicle wash using an FLx800 microplate fluorimeter (Bio-Tek Instrument, Inc. Winooski, Vermont) and comparing against a standard curve of known concentration and fluorescence. A syringe pump (Harvard Apparatus; Holliston, MA) was used to flow the suspension of nanobeads, vehicles, or microbubbles at the specified concentrations into the sample volume at a controlled rate of 1 or 6.35 mL/hr corresponding to a calculated wall shear stress of 3 or 20 dyn/cm^2, respectively.

An inverted microscope interfaced with a video camera allowed observation of the translation and adhesion of microbubbles and nanobeads within the tube. DiI fluorescence was used to determine the relative levels of lipid deposition. An ultrasonic transducer (Panametrics V305; Waltham, MA) was positioned in the water bath such that its acoustic focus corresponded to the optical focus of the microscope. The transducer was a 2.25 MHz center frequency, 0.75" element, 2" focus, single element transducer. The transducer had a -6 dB bandwidth of 1.5–3.3 MHz. An arbitrary waveform generator (AWG 2021, Tektronix, Inc.; Beaverton, OR) was

used to produce the custom waveforms combining radiation force administration and disruption of the agents. The ultrasound waveform consisted of a 1.3 second radiation force pulse at 3 MHz and 150 kPa peak negative pressure (PNP) and a 5-cycle fragmentation pulse at 1.5 MHz and 1.1 MPa PNP, as detailed in a previous manuscript [32]. A radio frequency power amplifier (3200L, ENI; Rochester, NY) amplified the signal approximately 55 dB for excitation of the transducer. Acoustic pressure calibrations and confocal optical and acoustic alignment were performed using a needle hydrophone (PZT-Z44-0400, Onda Corporation; Sunnyvale, CA) and a preamplifier (A17dB, Specialty Engineering Associates; Sunnyvale, CA) connected to a digital oscilloscope (9350, LeCroy; Chestnut Ridge, NY). Acoustically absorbent rubber was used to line the back wall of the water tank to eliminate standing waves and minimize reflections.

2.3 Image analysis

Video was obtained using the Pinnacle MovieBox and Studio version 9 software (Pinnacle; Mountain View, CA). Still images were obtained from the recorded video using the Studio software. These images were imported into a custom MATLAB 7.1 program (Mathworks, Natick, MA) which correlated the marker DiI (lipid) and nanobead fluorescence, converted them into masks, determined the pixel area, and calculated the percent overlap between the nanobead and lipid fluorescence.

2.4 Statistics

Graphs were generated and statistical analysis was performed using Graphpad Prism 4.0. Statistical analysis on the data was executed using an unpaired one-tailed t-test. Significance was determined as $p<0.05$.

3. Results and Discussion

3.1 Characterization of delivery vehicle

The feasibility of the vehicle design was examined by first determining the distribution of the nanobeads on the surface of biotinylated microbubbles. Binding of the fluorescent nanobeads to the microbubble surface resulted in clusters of nanobeads bound to the surface of the microbubble (Fig. 3). Specifically, the nanobeads were detected as a fluorescent “web” around large, black, “bean” and hexagon-shaped lipid domains. Recent reports indicate that this phenomenon is the result of phase separation between the saturated diacyl phosphatidylcholine, which form the domains, and the PEG-grafted species [30,33,34]. Thus, it is possible to influence nanoparticle surface distribution through thermotropic and/or barotropic control of domain morphology.

A quantitative measure of the surface coating of the microbubbles by the nanobeads was determined by flow cytometry. The forward and side scatter plots show a similar size and granularity range for the vehicles coated with 40- or 200-nm diameter beads (Fig. 4a,b). Mean fluorescence intensities (MFI) were also similar for the vehicles coated with 40- and 200-nm diameter beads resulting in 198 and 180 MFI, respectively (Fig. 4c,d). The size distribution for the two vehicle populations were not significantly different (Fig. 4e,f). Additionally, the vehicle population distributions were not significantly different from microbubbles alone, suggesting that there was no significant vehicle aggregation. This was confirmed by microscopy (data not shown). Increases in forward scatter correlated with a concomitant increase in MFI demonstrating that the larger the microbubble, the greater its capacity to bind and present nanobeads on its surface regardless of bead diameter (Fig. 4g,h).

3.2 Targeted deposition of nanobeads using ultrasound radiation force

The ability of the vehicles to be displaced by USRF and adhere to the walls of a cylindrical tube in shear flow was tested. At a wall shear stress of 3 dyn/cm^2, a level commensurate with blood flow in venules, the ultrasound pulse sequence directed the vehicles to the tube surface and facilitated the local deposition of 40 nm beads on the tube wall (Fig. 5a,b). Accumulation of nanobeads on the tube surface increased between two and eight minutes of flow and continuous application of USRF. USRF was focused such that particles were deflected away from the transducer, resulting in accumulation of nanobeads on the far side of the tube.

The effect of various physical parameters on the efficiency of nanobead deposition by the delivery vehicles was examined. With a vehicle concentration of 10^6/ml, nanobead accumulation on the tube wall was rarely detected in the absence of USRF. Bead deposition was blocked to baseline in the presence of biotinylated mouse antibody (Fig. 6a). There was a 3-fold increase in 40 nm diameter bead adhesion between 2 and 8 minutes of insonation. A 10-fold increase in vehicle concentration correlated with a 5-fold increase in nanobead deposition after 2 minutes. There was a ~3-fold increase in nanobead capture after 8 minutes, suggesting that concentration in the tube is more critical than insonation time for nanobead deposition. An increase in the wall shear stress up to 20 dyn/cm^2 prevented most deposition of 200 nm nanobeads on the tube wall, but did not significantly diminish recruitment of the smaller nanobeads. Thus, the use of smaller nanobeads could enable deposition to vasculature under high shear stress.

As a control, the deposition of neutravidin nanobeads alone in fluid shear (3 dyn/cm^2) was compared to ultrasound-mediated nanobead deposition by vehicles (Figure 6b). The nanobead concentrations applied ($3.6x10^{12}$/ml for 40 nm and $8.6x10^8$/ml for 200 nm nanobeads) were over 10-fold larger than the concentration that bound to the microbubbles. For both 40 nm and 200 nm beads (not initially bound to vehicles), there was no significant difference between ultrasound treated and untreated regions of the tube. Quantification of a similar tube area demonstrated a 4-fold greater deposition of 40 nm nanobeads by the vehicles than by nanobeads alone. Given that the concentration of injected nanobeads was an order of magnitude greater in the nanobeadalone case, the efficiency of bead deposition on the wall is much greater for the vehicles than for nanobeads alone. Additionally, in the nanobeadalone samples, the tubes were similarly coated with nanobeads throughout the length of the entire tube after 8 minutes whereas vehicle deposition of nanobeads was limited to the tube area defined by the ultrasound focal zone. These results suggest that nanoparticle-loaded microbubbles can increase the therapeutic index of a drug by, (i) reducing the non-specific interactions between the substrate and the nanobeads and (ii) depositing more material in the target region than by flow alone. Together these data demonstrate that USRF driven molecular targeting of nanobeads using a microbubble carrier vehicle is site specific and dependent upon the concentration of vehicles, wall shear stress, nanoparticle size, and the time of insonation.

3.3 Lipid shell remains bound to particles

Following microbubble destruction, portions of the lipid shell of the microbubble remain attached to the bound nanobeads after insonification, as evidenced by remaining DiI fluorescence. 80% of the wall on which lipid was deposited colocalized with bound nanobeads (Fig. 7a). Deposition of 40 nm and 200 nm beads colocalized with lipid fluorescence in ~80% and 50% of the imaged area, respectively. No significant difference was observed in the total area of lipid deposited by insonated vehicles as a function of the nanobead diameter (Fig. 7b). As an additional control, biotinylated lipid deposition was measured in the absence of nanobeads. For a similar concentration of microbubbles (10^6/ml) and after 8 minutes of insonation, lipid deposition was over 2-fold greater for avidin-coated microbubbles than those with nanobeads. This deposition could be inhibited to baseline levels by pre-incubation with

biotinylated mouse antibody. The observation that the lipid shell remain attached to the deposited nanobeads enables the incorporation of distinct compounds on the lipid and the nanoparticle. In this manner two different types of drugs could be co-delivered at defined concentrations.

4. Conclusions

A novel method of targeted particle deposition is presented using microbubbles coupled to ligand-coated nanoparticles to combine USRF targeting with specific receptor-ligand complexes. The results using a model system demonstrated that: 1) avidinated nanobeads coat the surface of biotinylated microbubbles heterogeneously; thereby presenting high density domains of the bound nanobeads and thus concentrated regions of ligand; 2) movement of microbubbles using USRF is not disrupted by bound nanobeads; 3) USRF can be used to direct the model drug delivery vehicles to the biotinylated tube surface and locally deposit nanobeads to the tube wall within a precise area determined by the focal zone of the transducer; 4) accumulation of nanobeads on the tube wall was molecularly specific and could be focused by the use of USRF; and 5) the specific deposition of nanobeads using this vehicle was hierarchically dependent upon vehicle concentration, wall shear stress, nanobead size, and length of insonation. This methodology holds promise for future application as a multi-functional multi-drug delivery vehicle for the treatment of many diverse diseases.

Acknowledgements

This research was supported by NIH R01 CA 103828. We would like to thank Hanako Zeidenberg, Eric Paoli and Erika Little for their assistance with the analysis and quantification of the binding experiments. We would also like to thank Charles Caskey for his assistance with experimental setups and Erika Little for manuscript formatting and editing.

References

1. Moghimi SM, Hunter AC, Murray JC. Long-circulating and target-specific nanoparticles: Theory to practice. Pharmacol Rev 2001;53(2):283–318. [PubMed: 11356986]
2. Jain RK. Transport of molecules across tumor vasculature. Cancer Metastasis Rev 1987;6(4):559–593. [PubMed: 3327633]
3. Matsumura Y, Maeda H. A new concept for macromolecular therapeutics in cancer chemotherapy: mechanism of tumoritropic accumulation of proteins and the antitumor agent smancs. Cancer Res 1986;46(12 Pt 1):6387–6392. [PubMed: 2946403]
4. Maeda H. The enhanced permeability and retention (EPR) effect in tumor vasculature: the key role of tumor-selective macromolecular drug targeting. Adv Enzyme Regul 2001;41:189–207. [PubMed: 11384745]
5. Garver MK, Weyrich AS, Li W, Lorant DE. Decreased transendothelial cell migration in neonates is associated with delayed expression of P-selectin. Pediatr Res 1996;39:295A. [PubMed: 8825803]
6. Horton MA. The alpha v beta 3 integrin “vitronectin receptor”. Int J Biochem Cell Biol 1997;29(5): 721–725. [PubMed: 9251239]
7. Korpanty G, Grayburn PA, Shohet RV, Brekken RA. Targeting vascular endothelium with avidin microbubbles. Ultrasound Med Biol 2005;31(9):1279–1283. [PubMed: 16176794]
8. G.E. Weller, F.S. Villanueva, E.M. Tom, W.R. Wagner, Targeted ultrasound contrast agents: In vitro assessment of endothelial dysfunction and multi-targeting to ICAM-1 and sialyl Lewis(x), Biotechnol. Bioeng. (2005), epub ahead of print.
9. Takalkar AM, Klibanov AL, Rychak JJ, Lindner JR, Ley K. Binding and detachment dynamics of microbubbles targeted to P-selectin under controlled shear flow. J Control Release 2004;96(3):473–482. [PubMed: 15120903]
10. Rychak JJ, Klibanov AL, Hossack JA. Acoustic radiation force enhances targeted delivery of ultrasound contrast microbubbles: in vitro verification. IEEE Trans Ultrason Ferroelectr Freq Control 2005;52(3):421–433. [PubMed: 15857050]

11. Zhao S, Borden M, Bloch SH, Kruse D, Ferrara KW, Dayton PA. Radiation-force assisted targeting facilitates ultrasonic molecular imaging. Mol Imaging 2004;3(3):135–148. [PubMed: 15530249]
12. Unger EC, Porter T, Culp W, Labell R, Matsunaga T, Zutshi R. Therapeutic applications of lipid-coated microbubbles. Adv Drug Deliv Rev 2004;56(9):1291–1314. [PubMed: 15109770]
13. Chao TC, Wang WS, Yen CC, Chiou TJ, Liu JH, Chen PM. A dose-escalating pilot study of sterically stabilized, pegylated liposomal doxorubicin (Lipo-Dox) in patients with metastatic breast cancer. Cancer Invest 2003;21(6):837–847. [PubMed: 14735687]
14. Fritz TA, Unger EC, Sutherland G, Sahn D. Phase I clinical trials of MRX-115. A new ultrasound contrast agent. Invest Radiol 1997;32(12):735–740. [PubMed: 9406013]
15. Klibanov AL. Targeted delivery of gas-filled microspheres, contrast agents for ultrasound imaging. Adv Drug Deliv Rev 1999;37(1–3):139–157. [PubMed: 10837732]
16. Takeuchi H, Kojima H, Yamamoto H, Kawashima Y. Evaluation of circulation profiles of liposomes coated with hydrophilic polymers having different molecular weights in rats. J Control Release 2001;75(1–2):83–91. [PubMed: 11451499]
17. Papahadjopoulos D, Allen TM, Gabizon A, Mayhew E, Matthay K, Huang SK, Lee KD, Woodle MC, Lasic DD, Redemann C, et al. Sterically stabilized liposomes: improvements in pharmacokinetics and antitumor therapeutic efficacy. Proc Natl Acad Sci USA 1991;88(24):11460–11464. [PubMed: 1763060]
18. Klibanov AL, Maruyama K, Torchilin VP, Huang L. Amphipathic polyethyleneglycols effectively prolong the circulation time of liposomes. FEBS Lett 1990;268(1):235–237. [PubMed: 2384160]
19. Allen TM, Hansen C, Martin F, Redemann C, Yau-Young A. Liposomes containing synthetic lipid derivatives of poly(ethylene glycol) show prolonged circulation half-lives in vivo. Biochim Biophys Acta 1991;1066(1):29–36. [PubMed: 2065067]
20. Ishida T, Harada M, Wang XY, Ichihara M, Irimura K, Kiwada H. Accelerated blood clearance of PEGylated liposomes following preceding liposome injection: Effects of lipid dose and PEG surface-density and chain length of the first-dose liposomes. J Control Release 2005;105(3):305–317. [PubMed: 15908032]
21. Daemen T, Hofstede G, Ten Kate MT, Bakker-Woudenberg IA, Scherphof GL. Liposomal doxorubicin-induced toxicity: depletion and impairment of phagocytic activity of liver macrophages. Int J Cancer 1995;61(5):716–721. [PubMed: 7768646]
22. Hubert A, Lyass O, Pode D, Gabizon A. Doxil (Caelyx): an exploratory study with pharmacokinetics in patients with hormone-refractory prostate cancer. Anticancer Drugs 2000;11(2):123–127. [PubMed: 10789595]
23. Harrison M, Tomlinson D, Stewart S. Liposomal-entrapped doxorubicin: an active agent in AIDS-related Kaposi's sarcoma. J Clin Oncol 1995;13(4):914–920. [PubMed: 7707119]
24. Halm U, Etzrodt G, Schiefke I, Schmidt F, Witzigmann H, Mossner J, Berr F. A phase II study of pegylated liposomal doxorubicin for treatment of advanced hepatocellular carcinoma. Ann Oncol 2000;11(1):113–114. [PubMed: 10690399]
25. Goebel FD, Goldstein D, Goos M, Jablonowski H, Stewart JS. Efficacy and safety of Stealth liposomal doxorubicin in AIDS-related Kaposi's sarcoma. The International SL-DOX Study Group. Br J Cancer 1996;73(8):989–994. [PubMed: 8611437]
26. V.F.K. Bjerknes, Fields of Force, Columbia University Press, New York, 1906
27. Dayton PA, Allen JS, Ferrara KW. The magnitude of radiation force on ultrasound contrast agents. J Acoust Soc Am 2002;112(5 Pt 1):2183–2192. [PubMed: 12430830]
28. Dayton PA, Morgan KE, Klibanov ALS, Brandenburger G, Nightingale KR, Ferrara KW. A preliminary evaluation of the effects of primary and secondary radiation forces on acoustic contrast agents. IEEE Trans Ultrason Ferroelectr Freq Control 1997;44(6):1264–1277.
29. Dayton P, Klibanov A, Brandenburger G, Ferrara K. Acoustic radiation force in vivo: A mechanism to assist targeting of microbubbles. Ultrasound Med Biol 1999;25(8):1195–1201. [PubMed: 10576262]
30. Borden MA, Dayton PA, Zhao S, Ferrara KW. Physicochemical Properties of the Microbubble Lipid Shell: Composition, Microstructure & Properties of Targeted Ultrasound Contrast Agents. IEEE Ultrason Symp 2004:20–23.

31. Klibanov AL. Ligand-carrying gas-filled microbubbles: ultrasound contrast agents for targeted molecular imaging. Bioconjug Chem 2005;16(1):9–17. [PubMed: 15656569]

32. Shortencarier MJ, Dayton PA, Bloch SH, Schumann PA, Matsunaga TO, Ferrara KW. A method for radiation-force localized drug delivery using gas-filled lipospheres. IEEE Trans Ultrason Ferroelectr Freq Control 2004;51(7):822–831. [PubMed: 15301001]

33. Borden MA, Pu G, Runner GJ, Longo ML. Surface phase behavior and microstructure of lipid/PEG-emulsifier monolayer-coated microbubbles. Colloids Surf B-Biointerfaces 2004;35(3–4):209–223. [PubMed: 15261034]

34. Borden MA, Kruse DE, Caskey CF, Zhao S, Dayton PA, Ferrara KW. Influence of lipid shell physicocehmical properties on ultrasound-induced microbubble destruction. IEEE Trans UFFC 2005;25(11):1992–2002.

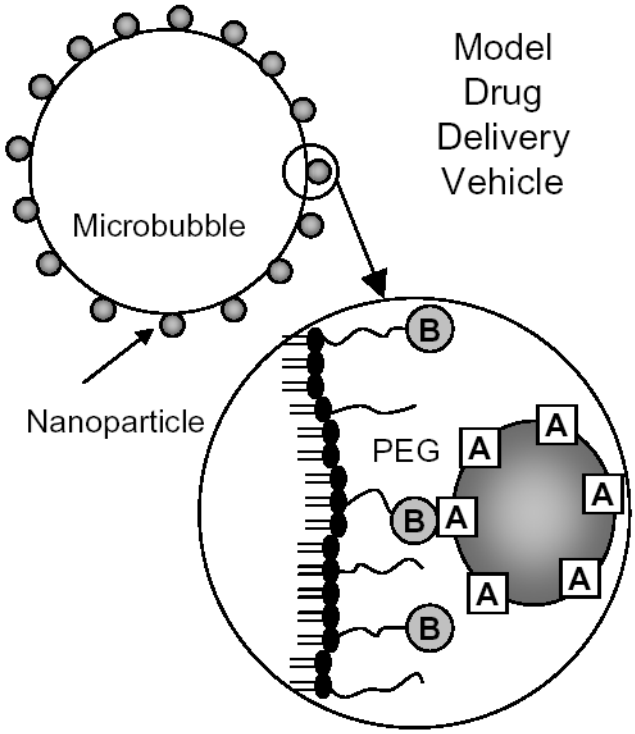

Fig. 1.

The design of a model drug delivery vehicle. A lipid-monolayer shelled microbubble is coated with both PEG and PEG-biotin (B). Subsequently, fluorescent nanobeads are coupled via neutravidin (A) to model a drug carrier as well as providing a fluorescent measure to determine surface distribution and adhesion. Neutravidin is presented on the surface of the vehicle on the nanobeads enabling molecular targeting of biotin.

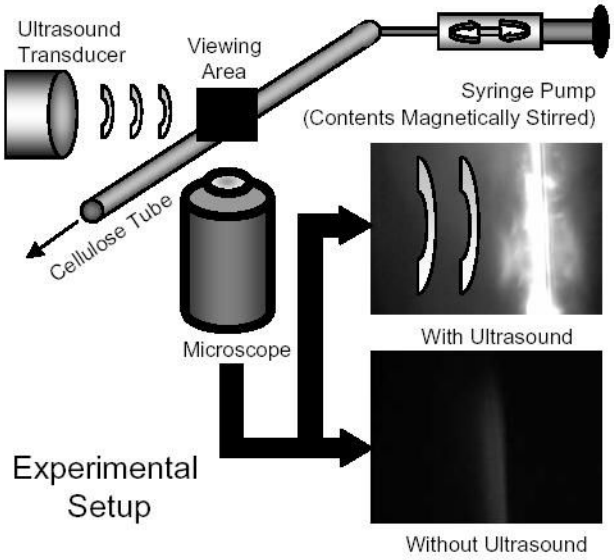

Fig. 2.

A diagram of the experimental setup. A water bath is mounted onto an inverted microscope and the ultrasound transducer is submerged and calibrated within the focal plane using a hydrophone. A 200-μm diameter cellulose tube coated with biotin is used as the test vessel. Vehicles are diluted in a syringe to a concentration of ~10^6 or 10^7 vehicles/ml and injected into the system using a syringe pump at a flow rate of 1 or 6.35 ml/hr corresponding to a wall shear stress of 3 or 20 dyn/cm^2. Without USRF, microbubbles remain within the bulk flow. However, upon application of USRF, microbubbles are pushed into the apposing side of the tube from the ultrasound transducer. Adhesion of nanobeads and lipid to the side of the tube was observed using a CCD camera and recorded digitally using computer video capture.

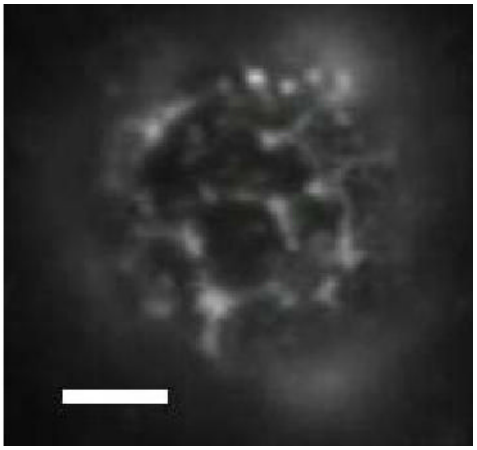

Fig. 3.

Nanobead distribution on the surface of the vehicles. Vehicles were created as described in Materials and Methods. A sample of the vehicle solution was observed on a 100X water immersion objective. The fluorescence within the image is yellow-green fluorescence emitted by the nanobeads bound to the microbubble surface. The scale bar corresponds to 5 microns in length.

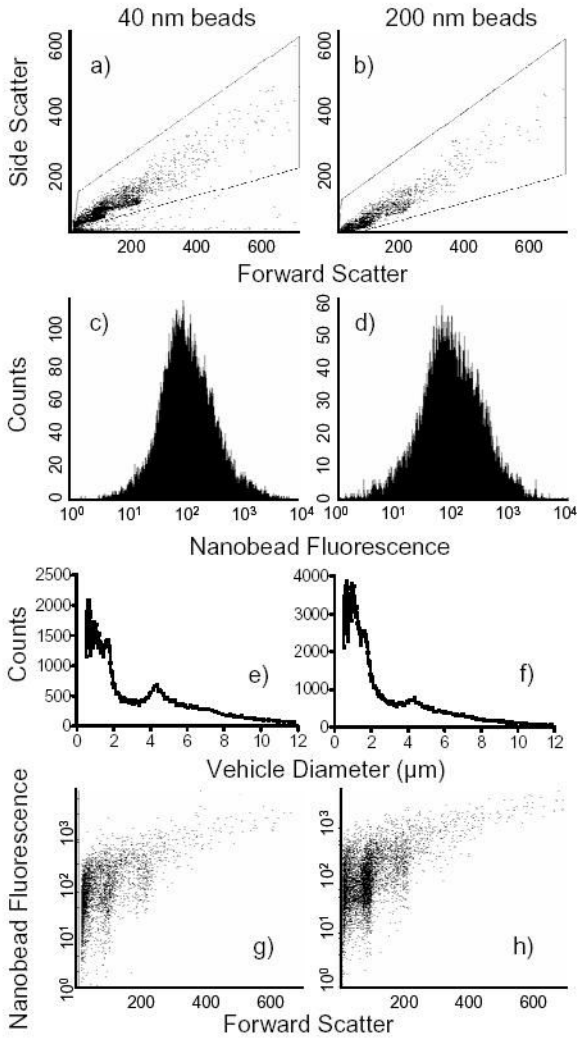

Fig. 4.

Characterization of the vehicles. A flow cytometric analysis of nanobead coverage of microbubbles was conducted using a FACScan flow cytometer. (a) The dot plots demonstrate the forward and side light scatter of the vehicles which correspond to relative size and granularity, respectively. (b) The fluorescence histogram plot registers only those particles which fall within the gate in the previous dot plots. From this population, a mean fluorescence intensity (MFI) can be determined which correlates with the number of nanobeads bound. (c) The vehicle size distribution was determined by an Accusizer. Each graph represents three separate samples of the respective vehicles. (d) Plotting forward light scatter against fluorescence allows the observation of size versus fluorescent nanobead binding, respectively.

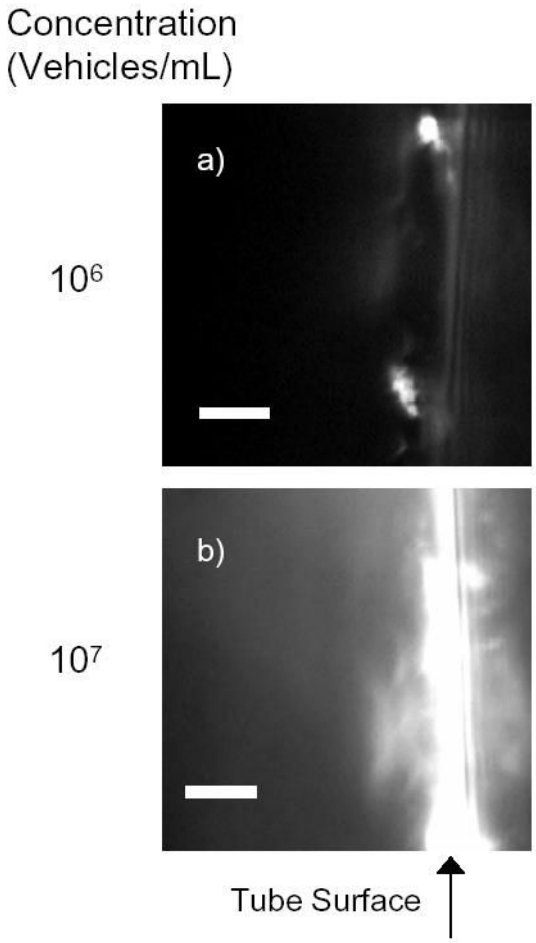

Fig. 5.

Deposition of fluorescent avidin-coated nanobeads on the surface of a biotinylated cellulose tube. This is an example of the microcopy of USRF induced nanobead deposition on biotin-coated cellulose tube surface at two different vehicle concentrations, (a) 10^6 vehicles/ml and (b) 10^7 vehicles/ml. Vehicles were prepared and flowed through a biotin-coated cellulose tube as described in Materials and Methods. The images shown represent one out of many focal views after 8 minutes of insonation. The scale bar corresponds to 5 microns in length.

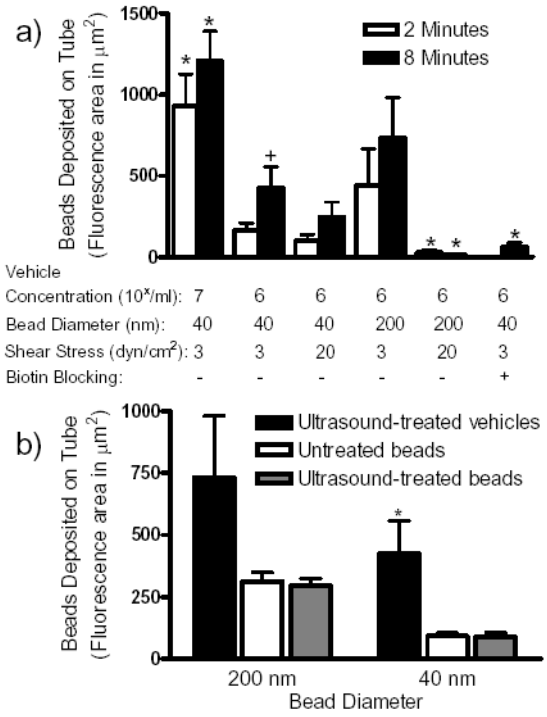

Fig. 6.

Quantification of the deposition of fluorescent avidin-coated nanobeads on the surface of a biotinylated cellulose tube. (a) Data were collected with varied concentration, wall shear stress, and length of insonation. Each set of samples represents the total area of deposition (in μm^2) per sample (mean ± SEM) for up to 10 samples. '*' represents significance over the control samples with respect to time of insonation (10^6/mL, 3 dyn/cm^2, 40 nm diameter nanobead samples) while '+' represents a significance difference between the respective time point for $p<0.05$. (b) The samples presented were sheared at 3 dyn/cm^2 for at least 8 minutes with or without insonation. Vehicle concentrations were 10^6/ml. Bead concentrations for 40 nm were $3.6x10^{12}$/ml and for 200 nm were $8.6x10^8$/ml. All experiments were conducted with insonation, however, the untreated bead samples were observed along an insonated tube distant from the focus of the ultrasound. Each set of samples represents the total area of deposition (in μm^2) per sample (mean ± SEM) for up to 10 samples. '*' represents significance over the control samples for $p<0.05$.

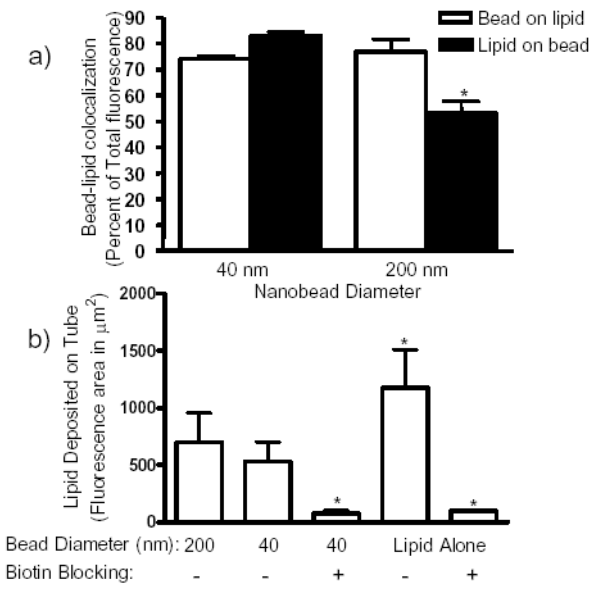

Fig. 7.

Lipid deposition coinciding with nanobead adherence. (a) Co-localized binding of microbubble lipid shell with nanobeads was observed, quantified, and presented as the percent of co-localization (mean ± SEM). '*' represents a significance difference with respect to nanobead size for $p<0.05$. (b) Quantification of lipid accumulation, using the lipophilic marker DiI, on the cellulose tube surface was conducted similarly to the nanobead fluorescence analysis above. Each set of samples represents the total area of deposition (in μm^2) per sample (mean ± SEM) for up to 10 samples after 8 minutes of insonation. '*' represents significance over the control sample for $p<0.05$.